Harmonic Emission Modelling of Electric Vehicle Chargers

Liang, Yawen; Wang, Lu; Qin, Zian; Bauer, Pavol

DOI
10.1109/IECON49645.2022.9968654

Publication date
2022

Document Version
Final published version

Published in
IECON 2022 - 48th Annual Conference of the IEEE Industrial Electronics Society

IECON 2022 – 48th Annual Conference of the IEEE Industrial Electronics Society | 978-1-6654-8025-3/22/$31.00 ©2022 IEEE | DOI: 10.1109/IECON49645.2022.9968654

Harmonic Emission Modelling of Electric Vehicle Chargers

Yawen Liang
Delft University of Technology
Delft, The Netherlands
Y.LIANG-12@student.tudelft.nl

Lu Wang
Delft University of Technology
Delft, The Netherlands
L.Wang-11@tudelft.nl

Zian Qin
Delft University of Technology
Delft, The Netherlands
Z.Qin-2@tudelft.nl

Pavol Bauer
Delft University of Technology
Delft, The Netherlands
P.Bauer@tudelft.nl

***Abstract*—In emerging fast-charging stations, DC fast chargers (DCFCs) are employed which rely on power electronics and control to achieve the required performance. Harmonic emission induced by the complex system behavior is of great concern in the DCFC system. This paper proposes a harmonic emission model for the typical electric vehicle charger design, i.e., two-level active front end. The technique is based on the Fourier series method and the impedance model which is able to reveal the harmonic current emission of DCFCs under different grid conditions. Time-domain simulations are presented subsequently to validate the proposed model.**

***Index Terms*—DC fast charger, harmonics, Fourier series, impedance model**

I. Introduction

With the roll-out of electric vehicles (EVs), a massive installation of fast-charging stations (FCSs) is expected [1]. However, same as wind turbine inverters and PV inverters [2, 3], DC fast chargers (DCFCs) installed in FCSs are essentially power electronic based devices leading to power quality degradation because of their harmonic current emission [4]. Thus, harmonic emission modelling is essential for analysing the root cause of DCFCs' harmonic emission, which avails the design of DCFCs to prevent severe harmonic issues.

A typical DCFC consists of several power modules. In each module, an AC/DC and a DC/DC converter are enclosed. The harmonic emission of the DCFC is mainly determined by the AC/DC converter [5]. For the AC/DC converter, one of the typical designs, i.e., two-level active front end (AFE), which is considered in this paper, is illustrated in Fig. 1.

Harmonic spectrum for the two-level converter has been discussed based on double Fourier series method in literature [6–8]. However, most of them focus only on high frequencies. The low order harmonics are thought to be easily eliminated by current control [9]. However, such neglect of low order harmonics may be incorrect when the low order harmonics are amplified because of the resonance in a charger-grid system.

Hence, a harmonic emission model mainly considering low-frequency harmonics is proposed in this paper. In section II, the analytical modelling of the harmonic emission for a two-level AFE is elaborated. In section III, a comparison between simulation and theoretical calculation is given. Section IV gives conclusions of this paper.

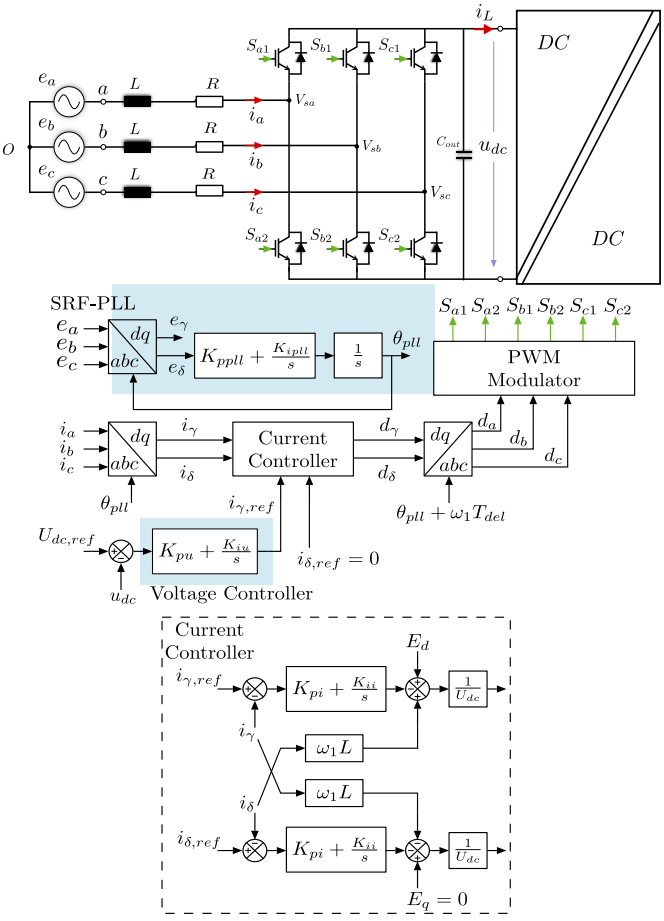

Fig. 1. Active front-end converter of the DCFC with the control block diagram.

II. Harmonic Current Emission Modelling for the AC/DC Converter

One effective technique for harmonic emission analysis is the impedance based method [10–13]. The impedance model of the charger-grid system is depicted in Fig. 2. The DCFC is modelled as a harmonic current source I_c in parallel with the converter input impedance Z_c. The grid is simplified as a background voltage source V_g in series with the grid impedance Z_g.

Based on the the model shown in Fig. 2, the harmonic current emission I_{e} under different grid conditions can be expressed as (1). The analytical model of the AC/DC converter input impedance Z_{c} is based on the small signal model (illustrated in Fig. 3) of the control block diagram shown in Fig. 1 while influences of the PLL dynamics, the inner current control loop, the outer voltage control loop and the fluctuation of DC-link voltage are taken into account.

$$I_e(s) = \frac{Z_c(s)I_c(s)}{Z_c(s)+Z_g(s)} - \frac{V_g(s)}{Z_c(s)+Z_g(s)} \tag{1}$$

With the modelling of the AC/DC converter input impedance Z_{c}, the harmonic emission induced by the grid harmonic voltage can be estimated. However, when the grid voltages are ideal sinusoidal waveforms without harmonics, there are still current harmonics that exist in the input current of DCFC due to the harmonic current source I_{c}. This harmonic current source is determined by the topology, the modulation method, the power filter, the switching frequency, the dead time, and also the DC-link voltage ripple.

As illustrated in Fig. 1, i_{a}, i_{b}, and i_{c} are the AC phase currents, V_{sa}, V_{sb}, and V_{sc} are the switch node voltages which are determined by the state of switches. To analyse the low frequency current harmonics drawn by the AFE, it is essential to first acquire the expression of the switch node voltage which is used to obtain the Fourier series of the switch node voltage. Then current harmonic with order h can be derived from the h_{th} components of the switch node voltage.

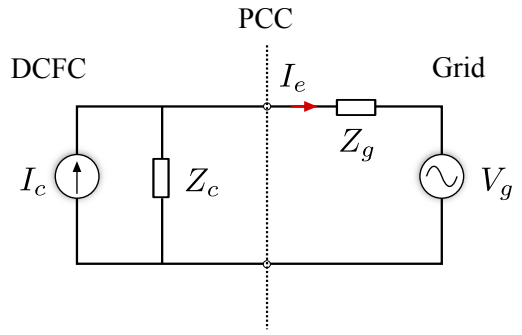

Fig. 2. Impedance model of a charger-grid system

A. Calculation of the switch node voltage

As shown in Fig. 4, the switch node voltage waveform can be expressed as (2),

$$V_{sa} = \begin{cases} U_{dc} & t \in (0,t_1),(t_2,t_3),\cdots,(t_N,T) \\ 0 & t \in (t_1,t_2),(t_3,t_4),\cdots,(t_{N-1},t_N) \end{cases} \tag{2}$$

Grounded on the principle of asymmetrical sampled modulation technique (shown in Fig. 4), the switching time instant can be established as following [14]. First, the wave angle y_{k} of the modulation waveform sampling time instant can be represented as,

$$y_k = \frac{\omega_1}{\omega_c}\pi(k-1) \quad k = 1,2,3,\cdots,N \tag{3}$$

where ω_1 is fundamental angular frequency, ω_c is angular frequency of triangular carrier, and $N = \frac{2\omega_c}{\omega_1}$. It should be noted that y_{k} is in reference to angle of the modulation waveform. Based on (3), the switching angle x_{k} can be derived as,

$$x_k = \frac{\pi}{2} + (k-1)\pi + (-1)^{(k+1)} \cdot \frac{\pi}{2} \cdot M \sin y_k \tag{4}$$

where M is the modulation index. In the next step, dead time effect on x_{k} is taken into consideration. The effect of the dead time t_{d} on the switch node voltages is demonstrated in Fig. 5, where the switching delay of the power switching devices is ignored [15].

It should be noted that the dead time effect on the switch node voltage (e.g. V_{sa}) depends on the polarity of the phase current (e.g., i_{a}). This yields the modified switching angle x_{k}^{*} as,

$$x_k^* = x_k + \frac{1 - sign(i)(-1)^k}{2} \cdot \omega_c T_d \tag{5}$$

where $sign(i) = 1$ if phase current $i_{\mathrm{a,b,c}} \geq 0$, $sign(i) = -1$ if phase current $i_{\mathrm{a,b,c}} < 0$, and T_{d} is the dead time period.

Apart from the previous analysis, the impact of actual waveforms of phase current (e.g. i_{a}, i_{b}, and i_{c}) needs to be taken into account. As shown in Fig. 6, the phase current i_{a} jumps between positive and negative in the initial phase of the modulation signal. On the one hand, $i_{\mathrm{a}} < 0$ during the first dead time period, which results in the switch node voltage V_{sa} being negative. On the other hand, $i_{\mathrm{a}} > 0$ during the second dead time period, which leads to a positive switch node voltage. Therefore, the actual switch node voltage around the starting point of the modulation signal is not affected by the dead time. This phenomenon also applies to switch node voltages in the final phase of the modulation signal.

To obtain the time period without dead time effects, the average model for the two-level AFE in Fig.1 is used,

$$\begin{cases} e_a = & L\frac{di_a}{dt} + Ri_a + U_{dc}(d_a - \frac{d_a+d_b+d_c}{3}) \\ e_b = & L\frac{di_b}{dt} + Ri_b + U_{dc}(d_b - \frac{d_a+d_b+d_c}{3}) \\ e_c = & L\frac{di_c}{dt} + Ri_c + U_{dc}(d_c - \frac{d_a+d_b+d_c}{3}) \end{cases} \tag{6}$$

where $d_{\mathrm{a,b,c}}$ is the phase leg average duty cycle [16]. The accurate phase current ripple shown in Fig. 6 can be obtained using (5). Therefore, the basic idea of time period T_{nd} without dead time effects calculation can be expressed as,

$$I_{average(a,b,c)}(T_{nd}) - \Delta I_{ripple(a,b,c)}(T_{nd}) = 0 \tag{7}$$

where $I_{\mathrm{average(a,b,c)}}$ is the phase current calculated by the average model in (6), and $\Delta I_{\mathrm{ripple(a,b,c)}}$ denotes the current ripple derived from the expression of $V_{\mathrm{sa,b,c}}$ and $e_{\mathrm{a,b,c}}$. Consequently, the switching time instant t_{k} within one fundamental period T can be finally obtained by the (8) and (9),

$$x_k^{**} = \begin{cases} x_k & t \in (t_0, t_0 + T_{nd1}) \\ x_k^* & t \in (t_0 + T_{nd1}, T - T_{nd2}) \\ x_k & t \in (T - T_{nd2}, T) \end{cases} \tag{8}$$

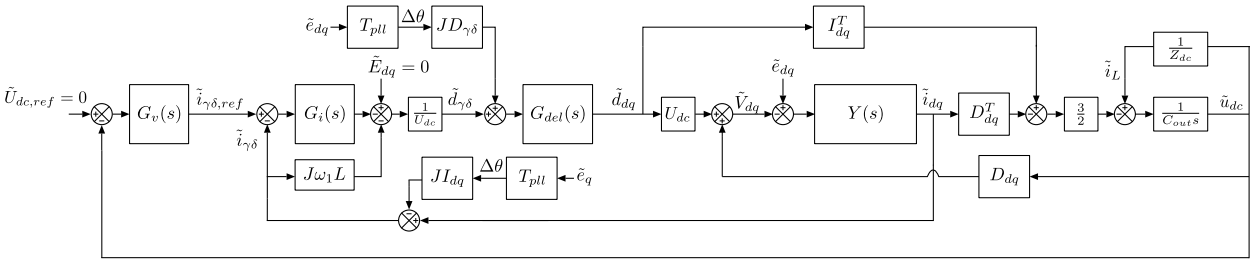

Fig. 3. Block diagram of the linearized small signal model of the system shown in Fig. 1

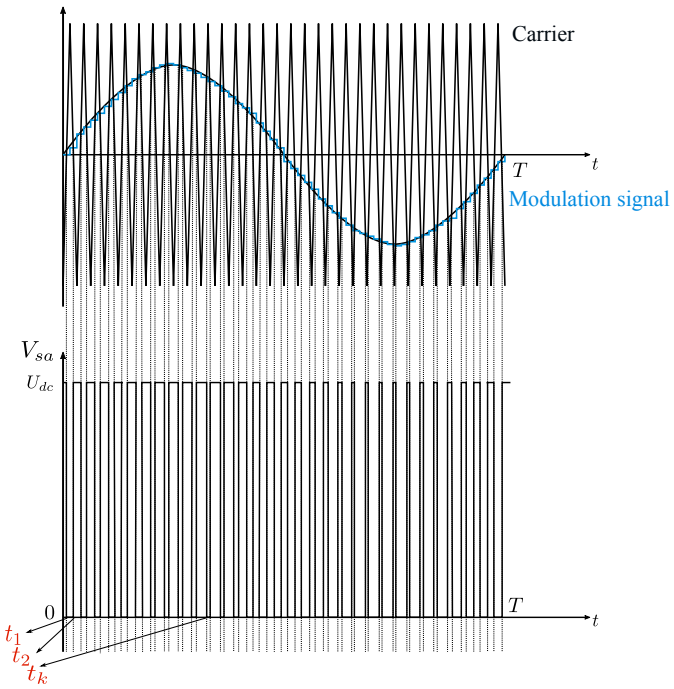

Fig. 4. The Principle of regular-sampled PWM technique (asymmetrically sampling).

where T_{nd1} is the first time period without dead time effects, and T_{nd2} is the second time period without dead time effects.

$$t_k = \frac{x_k^{**}}{N\pi} \times T_1 \tag{9}$$

where T_1 is the time period of fundamental waveform.

According to (2) and (9), coefficient a_{h} of Fourier series can be gained,

$$\begin{aligned} a_h &= \frac{2}{T}\int_{t_0}^{t_0+T} V_{sa}(t)\cos(\frac{2\pi}{T}\cdot ht)dt \\ &= \frac{U_{dc}}{h\pi}\sum_{k=1}^{N}\sin(\frac{2\pi}{T}\cdot ht_k)\cdot(-1)^{(k+1)} \end{aligned} \tag{10}$$

Coefficient b_{h} of Fourier series can be calculated in the same way,

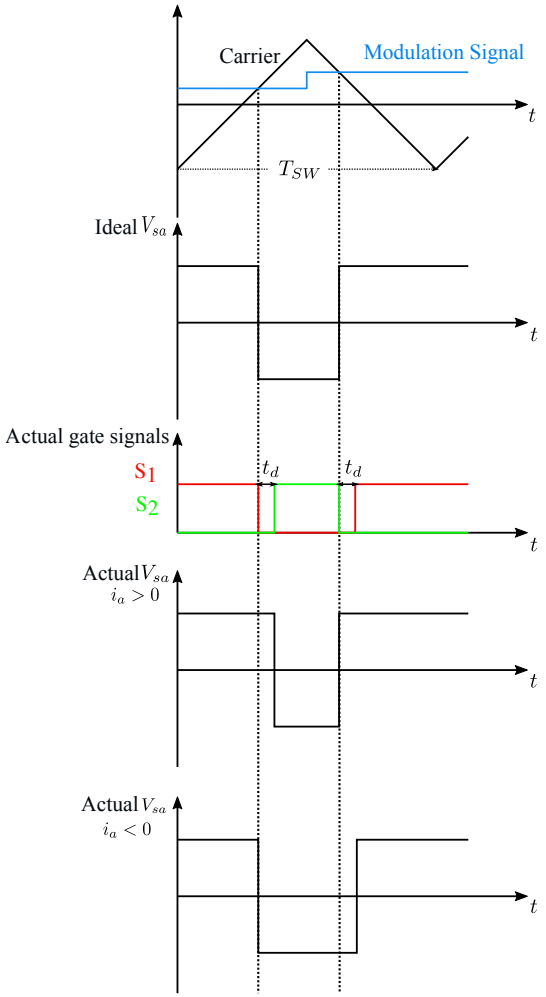

Fig. 5. Switch node voltage of Leg-A considering the dead time effect.

$$\begin{aligned} b_h &= \frac{2}{T}\int_{t_0}^{t_0+T} V_{sa}(t)\sin(\frac{2\pi}{T}\cdot ht)dt \\ &= \frac{U_{dc}}{h\pi}\sum_{k=1}^{N}\cos(\frac{2\pi}{T}\cdot ht_k)\cdot(-1)^{k} \end{aligned} \tag{11}$$

Based on (10) and (11), the h_{th} harmonics of the switch

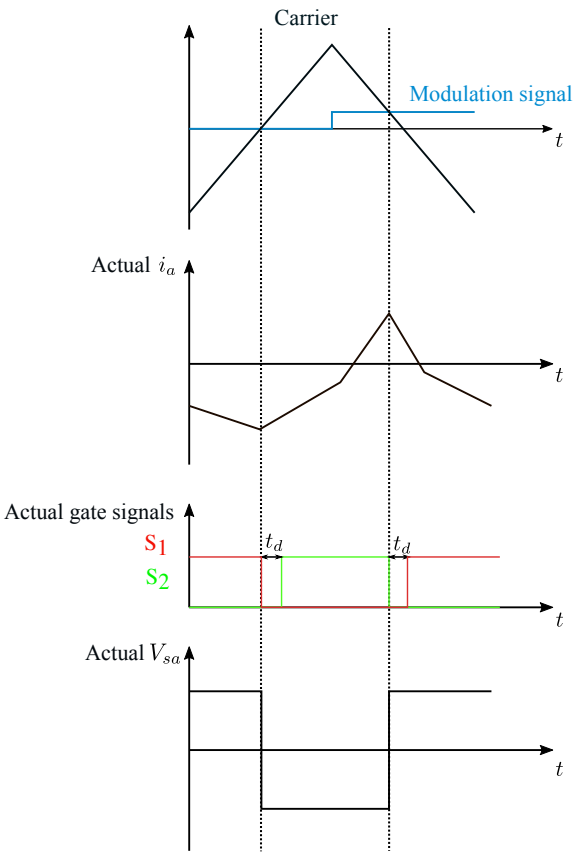

Fig. 6. Actual waveforms of phase current i_a, switch node voltage V_{sa} at the start point of one switching period.

node voltage (i.e., $V_{sa(h)}$, $V_{sb(h)}$, and $V_{sc(h)}$) can be obtained.

B. Calculation of current harmonics

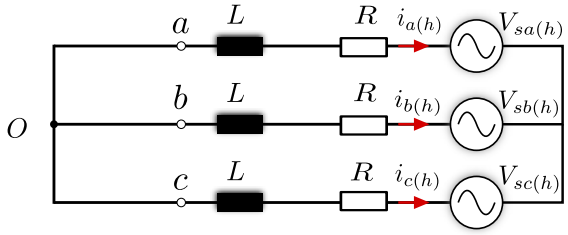

Fig. 7. Equivalent circuit of the active front-end.

According to the equivalent circuit in Fig. 7, the current harmonic of order h can be derived as,

$$i_{a(h)} = -\frac{(2V_{sa(h)} - V_{sb(h)} - V_{sc(h)})}{3(R + jh\omega L)} \tag{12}$$

where R is the resistance of the input filter, L is the inductance of the input filter, and h is the harmonic order. It is important to note that the grid voltages (i.e., e_a, e_b, and e_c) are assumed to be ideal sinusoidal waveform, which have no influence on the harmonics calculation.

In the previous calculation, only the modulation method and the dead time effects are taken into account. Regarding the high-frequency current harmonics exceeding controller bandwidth, control system effects can be ignored. However, this doesn't apply to the low-frequency current harmonics. To determine the low-frequency current harmonics induced by the control system and the DC-link voltage fluctuations, the open-loop current harmonics need to be integrated into the control block diagram to obtain the accurate values of the low-frequency harmonics in the input phase current $i_{a,b,c}$.

The final simplified block diagram of the system for closed-loop input current harmonics calculation is illustrated in Fig. 8, where the input $\tilde{i}_{dqDT}$ is $i_{a(h)}$ in (12), $\tilde{i}_{dq}$ is the harmonic current source I_e, $G_v(s)$ is the transfer function of the voltage controller, $G_{i2dctot}$ and $(1+G_{ol})^{-1}G_{ol}$ are the simplified blocks of the control diagram in Fig. 3 (expressed in (13) (14)).

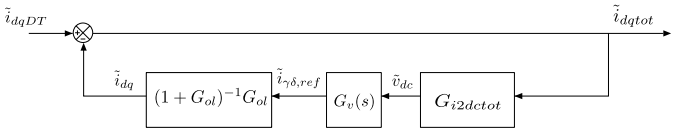

Fig. 8. Simplified block diagram of the linearized small signal model of the system

$$\begin{aligned}
G_{d2dc}(s) &= \frac{3}{2}\frac{1}{C_{out}s + \frac{1}{Z_{dc}}} I_{dq}^T \\
G_{i2dc}(s) &= \frac{3}{2}\frac{1}{C_{out}s + \frac{1}{Z_{dc}}} D_{dq}^T \\
G_{d2v}(s) &= U_{dc} + \frac{3}{2}\frac{1}{C_{out}s + \frac{1}{Z_{dc}}} D_{dq} I_{dq}^T \\
Z_{vdpasdq}(s) &= Y^{-1} + \frac{3}{2}\frac{1}{C_{out}s + \frac{1}{Z_{dc}}} D_{dq} D_{dq}^T \\
G_{i2dctot}(s) &= G_{i2dc} - G_{d2dc} G_{d2v}^{-1} Z_{vdpasdq}
\end{aligned} \tag{13}$$

$$\begin{aligned}
H(s) &= \frac{1}{U_{dc}} Z_{vdpasdq}^{-1} G_{d2v} G_{del} \\
H_{de}(s) &= (I - HJ\omega_1 L)^{-1} H \\
G_{ol}(s) &= H_{de} H_i
\end{aligned} \tag{14}$$

III. Simulation Validation

To verify the effectiveness of the harmonic emission model, time-domain simulations are conducted in PLECS Standalone. Parameters presented in Tables I and II are applied in the PLECS simulation.

Based on the analytical solution achieved in section II, calculation was carried out in Python to obtain the harmonic spectrums of input phase currents (i.e., i_a, i_b, and i_c). Low frequency harmonics including 5_{th}, 7_{th}, 11_{th}, and 13_{th} are selected for comparison since they are the most damaging frequency components to power devices and grid [17]. The results with different short circuit ratio (SCR) are shown in Fig. 9 and Fig. 10. It was found that the results achieved

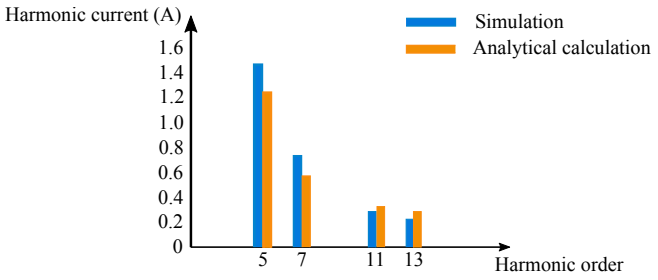

Fig. 9. The harmonic spectrum of input phase current (SCR=5).

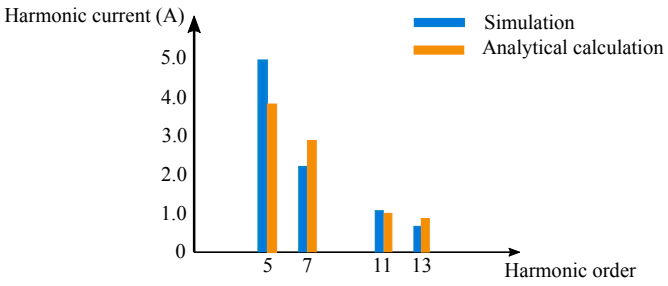

Fig. 10. The harmonic spectrum of input phase current (SCR=30).

TABLE I
CIRCUIT PARAMETERS OF THE AFE IN FIG. 1

Parameters	values
Grid voltage (line-to-neutral) V_g/V	230
Grid fundamental frequency f_1/Hz	50
Grid filter inductance L/μH	250
Grid filter resistance R/mΩ	20
DC-link voltage U_{dc}/V	800
Output capcitor V_{out}/μF	1500
AFE Switching frequency f_{sw}/kHz	40
AFE control sampling frequency f_s/kHz	80
AFE dead time T_d/μs	1
Reference modulation index M	0.40577494
Output power P_{out}/kW	30

TABLE II
CONTROLLER PARAMETERS OF THE AFE IN FIG. 1

Parameters	values
Proportional gain of current controller K_{pi}	1.256637
Integral gain of current controller K_{ii}	100.530965
Proportional gain of voltage controller K_{pu}	6.148755
Integral gain of current controller K_{iu}	254.664516
Proportional gain of SRF-PLL K_{ppll}	0.57950647
Integral gain of SRF-PLL K_{ipll}	109.23439616

with the proposed analytical model are matching the results achieved by the PLECS simulation well.

IV. CONCLUSION

This paper presents a harmonic emission model for the AFE in DCFCs, using the Fourier series and the impedance-based method. The analytical solution of the harmonic spectrum can be easily achieved using this model. First, the detailed harmonic emission modelling procedure is provided. Second, the calculation results from the developed model are compared with the time-domain simulation results to verify the validity of the model. It is shown that the calculation results of the analytical model are in good agreement with the simulation results. The derived model gives insight into the AFE's harmonics behavior in varying grid situations which can be applied to DCFCs' design.

REFERENCES

[1] L. Wang, Z. Qin, T. Slangen, P. Bauer, and T. van Wijk, "Grid impact of electric vehicle fast charging stations: Trends, standards, issues and mitigation measures - an overview," *IEEE Open Journal of Power Electronics*, vol. 2, pp. 56–74, 2021.

[2] J. Enslin and P. Heskes, "Harmonic interaction between a large number of distributed power inverters and the distribution network," *IEEE Transactions on Power Electronics*, vol. 19, no. 6, pp. 1586–1593, 2004.

[3] L. Beloqui Larumbe, Z. Qin, and P. Bauer, "Introduction to the analysis of harmonics and resonances in large offshore wind power plants," in *2018 IEEE 18th International Power Electronics and Motion Control Conference (PEMC)*, 2018, pp. 393–400.

[4] T. Thiringer and S. Haghbin, "Power quality issues of a battery fast charging station for a fully-electric public transport system in gothenburg city," *Batteries*, vol. 1, no. 1, pp. 22–33, 2015. [Online]. Available: https://www.mdpi.com/2313-0105/1/1/22

[5] L. Wang, Z. Qin, L. B. Larumbe, and P. Bauer, "Python supervised co-simulation for a day-long harmonic evaluation of ev charging," *Chinese Journal of Electrical Engineering*, vol. 7, no. 4, pp. 15–24, 2021.

[6] Z. Qin, H. Wang, F. Blaabjerg, and P. C. Loh, "Investigation into the control methods to reduce the dc-link capacitor ripple current in a back-to-back converter," in *2014 IEEE Energy Conversion Congress and Exposition (ECCE)*, 2014, pp. 203–210.

[7] J.Shen, J.A.Taufiq, and A.D.Mansell., "Analytical solution to harmonic characteristics of traction pwm converters," *IEE Proceedings - Electric Power Applications*, vol. 144, no. 2, pp. 158–168, 1997.

[8] H. Deng, L. Helle, Y. Bo, and K. B. Larsen, "A general solution for theoretical harmonic components of carrier based pwm schemes," in *2009 Twenty-Fourth Annual IEEE Applied Power Electronics Conference and Exposition*, 2009, pp. 1698–1703.

[9] T. Xu, F. Gao, X. Wang, T. Hao, D. Yang, and F. Blaabjerg, "Closed-loop elimination of low-order sideband harmonics in parallel-connected low-pulse ratio vsis," in *2018 IEEE Energy Conversion Congress and Exposition (ECCE)*, 2018, pp. 2271–2277.

[10] J. Sun, "Impedance-based stability criterion for grid-connected inverters," *IEEE Transactions on Power Electronics*, vol. 26, no. 11, pp. 3075–3078, 2011.

[11] B. Wen, D. Boroyevich, R. Burgos, P. Mattavelli, and Z. Shen, "Analysis of d-q small-signal impedance of grid-tied inverters," *IEEE Transactions on Power Electronics*, vol. 31, no. 1, pp. 675–687, 2016.

[12] J. Sun, "Small-signal methods for ac distributed power systems–a review," *IEEE Transactions on Power Electronics*, vol. 24, no. 11, pp. 2545–2554, 2009.

[13] X. Wang, L. Harnefors, and F. Blaabjerg, "Unified impedance model of grid-connected voltage-source converters," *IEEE Transactions on Power Electronics*, vol. 33, no. 2, pp. 1775–1787, 2018.

[14] N. Jiao, S. Wang, T. Liu, Y. Wang, and Z. Chen, "Harmonic quantitative analysis for dead-time effects in spwm inverters," *IEEE Access*, vol. 7, pp. 43 143–43 152, 2019.

[15] Y. Yang, K. Zhou, H. Wang, and F. Blaabjerg, "Analysis and mitigation of dead-time harmonics in the single-phase full-bridge pwm converter with repetitive controllers," *IEEE Transactions on Industry Applications*, vol. 54, no. 5, pp. 5343–5354, 2018.

[16] R. Lai, F. Wang, R. Burgos, D. Boroyevich, D. Jiang, and D. Zhang, "Average modeling and control design for vienna-type rectifiers considering the dc-link voltage balance," *IEEE Transactions on Power Electronics*, vol. 24, no. 11, pp. 2509–2522, 2009.

[17] P. S. Harmonics, "Power system harmonics: An overview," *IEEE Transactions on Power Apparatus and Systems*, vol. PAS-102, no. 8, pp. 2455–2460, 1983.